










COMMUNICATIONS CHEMISTRY

ARTICLE

<https://doi.org/10.1038/s42004-019-0216-2>

OPEN

Pressure-induced tuning of lattice distortion in a high-entropy oxide

Benyuan Cheng ^{1,2}, Hongbo Lou¹, Abhishek Sarkar ^{3,4}, Zhidan Zeng¹, Fei Zhang ^{1,5}, Xiehang Chen¹, Lijie Tan¹, Vitali Prakapenka⁶, Eran Greenberg ⁶, Jianguo Wen ⁷, Ruzica Djenadic^{3,9}, Horst Hahn ^{3,4} & Qiaoshi Zeng ^{1,8*}

As a new class of multi-principal component oxides with high chemical disorder, high-entropy oxides (HEOs) have attracted much attention. The stability and tunability of their structure and properties are of great interest and importance, but remain unclear. By using in situ synchrotron radiation X-ray diffraction, Raman spectroscopy, ultraviolet-visible absorption spectroscopy, and ex situ high-resolution transmission electron microscopy, here we show the existence of lattice distortion in the crystalline $(\text{Ce}_{0.2}\text{La}_{0.2}\text{Pr}_{0.2}\text{Sm}_{0.2}\text{Y}_{0.2})\text{O}_{2-8}$ HEO according to the deviation of bond angles from the ideal values, and discover a pressure-induced continuous tuning of lattice distortion (bond angles) and band gap. As continuous bending of bond angles, pressure eventually induces breakdown of the long-range connectivity of lattice and causes amorphization. The amorphous state can be partially recovered upon decompression, forming glass-nanoceramic composite HEO. These results reveal the unexpected flexibility of the structure and properties of HEOs, which could promote the fundamental understanding and applications of HEOs.

¹Center for High Pressure Science and Technology Advanced Research, Pudong, Shanghai 201203, P. R. China. ²Shanghai Institute of Laser Plasma, Shanghai 201800, P. R. China. ³Joint Research Laboratory Nanomaterials-Technische Universität Darmstadt and Karlsruhe Institute of Technology, 64287 Darmstadt, Germany. ⁴Institute of Nanotechnology, Karlsruhe Institute of Technology, 76344 Eggenstein-Leopoldshafen, Germany. ⁵State Key Laboratory for Advanced Metals and Materials, University of Science and Technology Beijing, Beijing 100083, P. R. China. ⁶Center for Advanced Radiation Sources, University of Chicago, Chicago, IL 60637, USA. ⁷Center for Nanoscale Materials, Argonne National Laboratory, Argonne, IL 60439, USA. ⁸Jiangsu Key Laboratory of Advanced Metallic Materials, School of Materials Science and Engineering, Southeast University, Nanjing 211189, P. R. China. ⁹Present address: Heraeus Deutschland GmbH & Co. KG, Heraeusstr. 12-14, 63450 Hanau, Germany. *email: zengqs@hpstar.ac.cn

To meet the rapidly evolving technology needs, the materials research community has been striving to seek new methodologies for advanced materials design. Increasing the number of components could effectively expand the configurational space for the exploration of novel materials. Recently, multiple principal components (>5) alloys, so-called high-entropy alloys (HEAs) have been successfully developed in metallic systems with solid solution phases. These HEAs are realized based on an idea with deliberately incorporating five or more elemental species into a single solid solution lattice with random site occupancy, which maximizes the configurational entropy to stabilize the system^{1–5}. Surprisingly, this high-entropy strategy also works for oxides with ionic bonds. Rost et al. first synthesized the transition metal ($\text{Mg}_{0.2}\text{Co}_{0.2}\text{Ni}_{0.2}\text{Cu}_{0.2}\text{Zn}_{0.2}$)O high-entropy oxide (HEO) with a rocksalt-type structure⁶. Subsequently, Djenadic et al. synthesized single CaF_2 -type phase rare-earth HEOs (RE-HEOs) $(\text{Ce}_{0.2}\text{La}_{0.2}\text{Pr}_{0.2}\text{Sm}_{0.2}\text{Y}_{0.2})\text{O}_{2-\delta}$ ⁷. More recently, complex HEOs with multiple cation Wyckoff positions, like perovskites^{8,9} or spinels¹⁰, have also been reported. HEOs provide great flexibility for element-based property design and engineering, therefore, have attracted extensive attention owing to their tremendous potential in various applications. Many remarkable properties of HEOs have been reported, including huge dielectric constant¹¹ and high room temperature Li ion conductivity¹², which have advanced several potential applications like defect dipoles¹³, epitaxial interface engineering¹⁴, and electrode materials in Li-ion battery^{15,16}.

High-entropy materials are also expected to possess ultrahigh structural stability due to their maximized configurational entropy in design (high-entropy effect), which could dramatically lower down the Gibbs free energy of the system. On the other hand, the high chemical disorder could induce severe lattice distortion which could raise the energy of the system. Therefore, it is compelling to experimentally clarify the stability and tunability of these novel materials under various conditions, which is crucial for our fundamental understanding of those new materials and also their potential applications^{17,18}. High-temperature is usually involved during the formation of single phase HEOs^{6,19}. Besides temperature, pressure is another fundamental parameter controlling the structure and properties of materials^{20–23}. Especially, for HEOs, the Gibbs energy ($G = PV - ST$), the local lattice distortion, the high-level oxygen vacancies, and even electronic states (valency) are all expected to be susceptible to pressure tuning, which, however, have not been explored before. Very recently, the seemingly ultra-stable HEAs have already been found to show rich polymorphism under high-pressure at room temperature. For example, pressure-induced irreversible polymorphic transitions from the *fcc* to *hcp* phases were observed in the prototype CoCrFeMnNi HEA^{24,25}, and a medium-entropy NiCoCrFe alloy²⁶; In another rare-earth system, an *hcp*-structured HoDyYGdTb HEA, more complex transitions following the sequence of *hcp* → Sm-type → *dhcp* → *dfcc* were reported²⁷; Even five polymorphs were discovered in the *bcc* $\text{Al}_{0.6}\text{CoCrFeNi}$ HEA^{18,28}. These results demonstrate that the HEAs are far more complex than expected as ultrastable solid solutions. Inspired by these recent results of HEAs, an intriguing question is raised: are the structure and properties tunable in HEOs?

In this work, we use in situ high-pressure synchrotron radiation X-ray diffraction (XRD), pair distribution function (PDF), Raman spectroscopy, and ex situ high-resolution transmission electron microscopy (HRTEM) to investigate the structural evolution of the rare earth $(\text{Ce}_{0.2}\text{La}_{0.2}\text{Pr}_{0.2}\text{Sm}_{0.2}\text{Y}_{0.2})\text{O}_{2-\delta}$ RE-HEO ((Ce,La,Pr,Sm,Y)O will be used hereafter for simplicity). Lattice distortion in the initial structure is confirmed by the slight deviation of bond angles from the ideal values. The bond angles are found to be extremely susceptible to pressure, which

continuously bend during compression and eventually causes a pressure-induced amorphization (PIA) in HEOs. The optical properties and band gap are also investigated through the transition by in situ high-pressure ultraviolet–vis (UV–vis) absorption spectroscopy, which shows interesting tunable behavior as well accompanying the structural change.

Results

Structure of the initial sample. (Ce,La,Pr,Sm,Y)O HEO powder samples were synthesized using nebulized spray pyrolysis (NSP) method⁷. The initial structure of the sample was characterized by chromatic-aberration corrected HRTEM and synchrotron radiation high-energy XRD. The experimental details are shown in the “Methods” section. HRTEM results (Supplementary Fig. 1) show that the sample has a particle size of $\sim 0.5 \mu\text{m}$, a crystalline grain size of $\sim 7 \text{ nm}$, and a CaF_2 -type (space group: *Fm-3m*) structure with its lattice parameter $a = 5.6 (1) \text{ \AA}$. The structure factor $S(q)$ obtained from the high-energy XRD with the moment transfer q coverage up to 30 \AA^{-1} is shown in Fig. 1a, the structure can be well indexed into a CaF_2 -type structure with a refined lattice parameter $a = 5.507(1) \text{ \AA}$. These results of the initial structure of the (Ce,La,Pr,Sm,Y)O HEO are consistent with the previous reports⁷. Fig. 1b shows the PDF data, $G(r)$, which was obtained by a Fourier transformation of the $S(q)$ data. Bond lengths can be accurately determined by fitting the peaks in $G(r)$, then, bond angles can be calculated. The initial average bond angles between oxygen and rare-earth elements, $\theta_{\text{RE-O-RE}}$ ($\sim 108.6^\circ$) and $\theta_{\text{O-RE-O}}$ ($\sim 68.3^\circ$), both are slightly smaller than the ideal values of a

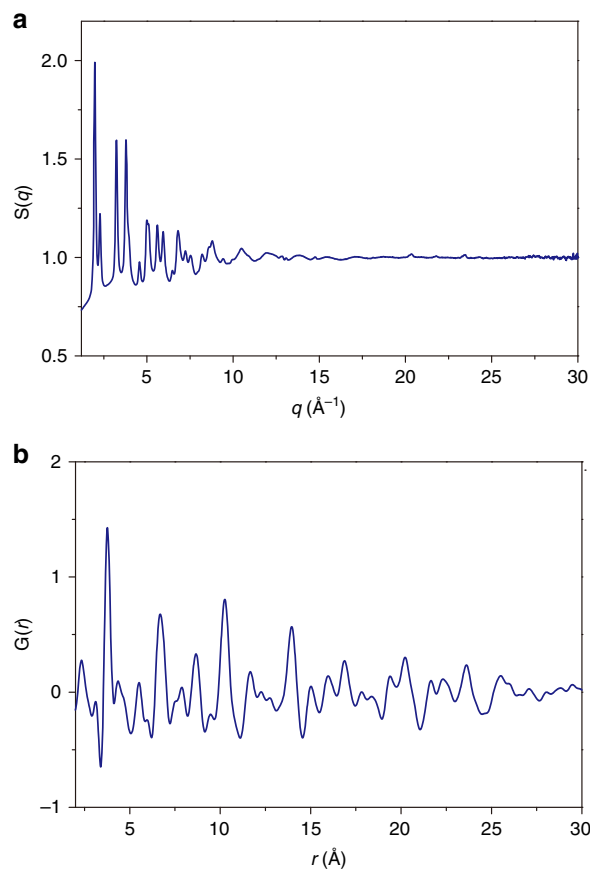


Fig. 1 High-energy XRD of the initial sample. The structure factor **a** and pair distribution function pattern **b** of the (Ce,La,Pr,Sm,Y)O HEO at ambient conditions obtained by high-energy X-ray diffraction. The X-ray wavelength was 0.1173 \AA . A transmission mode was used for the sample without any container

standard CaF_2 -type crystal structure ($\theta_{\text{RE-O-RE}} = 109.5^\circ$ and $\theta_{\text{O-RE-O}} = 70.5^\circ$), this is also consistent with the observation of smaller bond angles in the HRTEM results (Supplementary Fig. 1c), which may be attributed to the local lattice distortion in the (Ce,La,Pr,Sm,Y)O HEO. The lattice distortion could be caused by atomic size mismatch between neighboring RE elements, owing to the fact that cationic radii of the constituent rare-earth elements vary considerably, for example, from 0.97 Å (for Ce^{4+}) to 1.116 Å (for La^{3+}). Additionally, the high level of oxygen vacancies could also play an unneglectable role resulting in the observed lattice distortion²⁹.

In situ high-pressure XRD. To address the structural stability of the (Ce,La,Pr,Sm,Y)O HEO, its structural evolution up to ~31 GPa was monitored by in situ high-pressure synchrotron radiation XRD in a symmetric diamond anvil cell (DAC). A schematic illustration of a DAC is shown in Fig. 2a. Figure 2b presents the XRD patterns during compression and decompression. During compression, the initial CaF_2 -type structure loses its crystal coherence above ~16 GPa indicated by the disappearance of the initial sharp Bragg peaks and the emerging of amorphous-like broad peaks. The amorphous-like phase exists up to the highest pressure of ~31 GPa and seems recoverable to ambient pressure during decompression without the reappearance of the sharp Bragg peaks. The two-dimensional (2D) XRD images are shown in Supplementary Fig. 2.

Below 16 GPa, with increasing pressure, all the Bragg peaks of the initial CaF_2 -type structure shift to the larger two-theta values

below ~9 GPa simply due to the pressure-induced lattice shrinkage (Fig. 2c). At ~4 GPa, there is a slight slope change, and the peak position stops shifting above ~9 GPa. Below ~9 GPa, the intensity of all XRD peaks gradually but significantly weakens (Fig. 2d), and all the peak widths continuously increase as well (Fig. 2e). Both peak intensity and peak width show a slope change at ~4 GPa and become almost constant above 9 GPa. The peak intensity weakening and peak width increasing start at the very beginning of compression. This result indicates that the initial CaF_2 -type structure of the (Ce,La,Pr,Sm,Y)O HEO is susceptible to pressure and continuously becomes more and more disordered (topologically) during compression. Below ~16 GPa, the structure evolution has three stages (one till ~4 GPa, another between ~4 and ~9 GPa, and lastly above ~9 GPa) according to the peak position, intensity, and peak width changes as a function of pressure.

In situ high-pressure PDF. Since structural disordering occurs in the (Ce,La,Pr,Sm,Y)O HEO during compression, to derive more detailed information of the structural evolution, another experiment with larger Q coverage (up to 12 Å) was performed (more details are shown in the “Methods” section). The in situ high-pressure structure factor $S(q)$ was obtained after careful background subtracting and normalization (Fig. 3a). The peak position, intensity, and width of the $S(q)$ exhibit consistent behavior with the raw XRD data shown in Fig. 2. The peak intensity (Fig. 3b) and width (Fig. 3c) significantly change their slopes at ~16 GPa. Above ~30 GPa, smooth amorphous patterns are

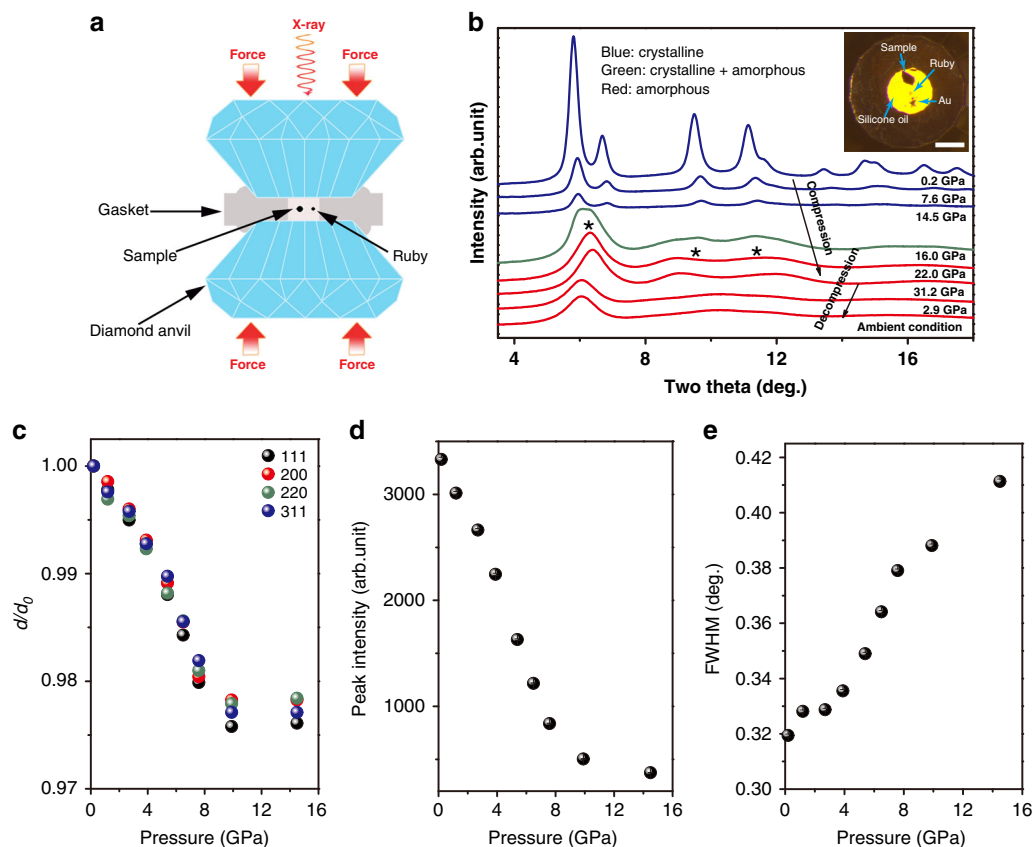


Fig. 2 In situ high-pressure XRD. **a** A schematic illustration of the DAC used to generate high-pressure. **b** Representative XRD patterns of (Ce,La,Pr,Sm,Y)O during compression and decompression at room temperature. Inset is an image of the sample loaded inside a DAC, the scale bar is 100 μm . The peaks of the amorphous phase are marked by asterisk symbols. The X-ray wavelength is 0.3218 Å. **c** Pressure dependence of d/d_0 of the CaF_2 -type cubic phase upon compression. Pressure dependence of the peak height **d** and peak width **e** of the (111) peaks (at -5.8°) upon compression

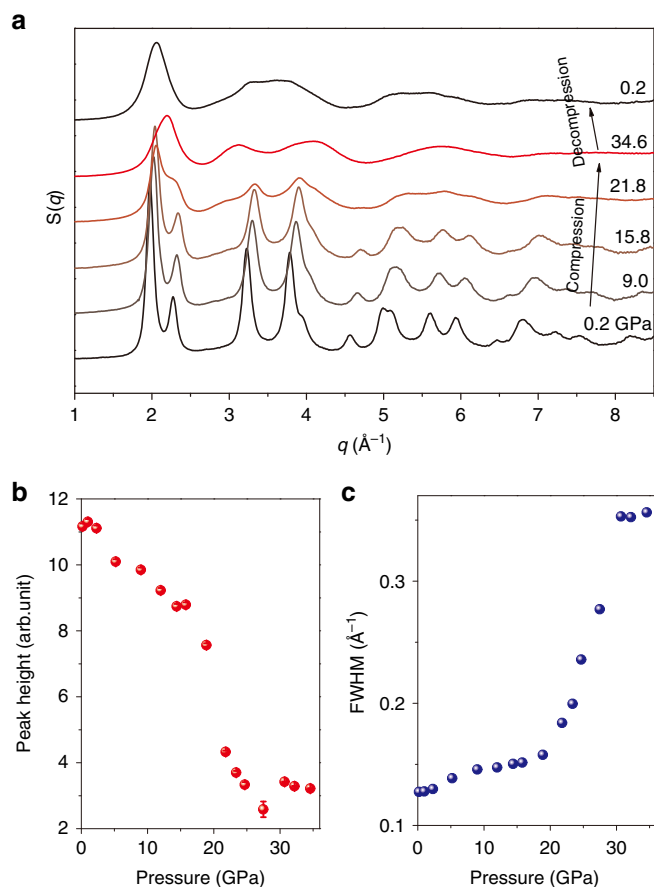


Fig. 3 Structure evolution in reciprocal space. **a** Selected structure factor of (Ce,La,Pr,Sm,Y)O HEO during compression and decompression at room temperature. **b** Pressure dependence of the peak height **b** and peak width **c** of the first sharp diffraction peak ($\sim 2.0 \text{ \AA}^{-1}$) upon compression

obtained. Meanwhile, the peak intensity and width do not change with pressure anymore, suggesting the completion of the amorphization process.

Structural information in real space is presented by PDF (Fig. 4a). Below ~ 20 GPa, the PDF patterns show strong oscillations without noticeable damping up to 25 \AA , which is a typical feature of crystalline materials with long-range translational symmetry. In contrast, above ~ 20 GPa, all the oscillations are significantly weakened and gradually smeared out above $\sim 10 \text{ \AA}$, which is in line with the amorphization process indicated by $S(q)$ data in reciprocal space. All the peaks of PDF which correspond to the distances between different atom pairs shift to smaller r values with increasing pressure below ~ 16 GPa. For convenience, the first nine peaks (illustrated in Fig. 4b) of the initial CaF_2 structure are denoted as P_1 – P_9 in Fig. 4a. Some peaks gradually weaken and merge into one new broad peak during compression, e.g., P_1 and P_2 , P_4 and P_5 . Above ~ 20 GPa, only four broad and weak peaks remain due to amorphization. The changes of the nine peak positions, the calculated atomic pair distances, and bond angles are shown in Fig. 5. The atomic pair distances shrink quite consistently below ~ 4 GPa, and then diverge at higher pressures, which could be the reason for the slight slope change at ~ 4 GPa observed in Fig. 2c–e. It should be noted that although the q coverage in the in situ high-pressure PDF measurement is limited ($q_{\text{max}} \approx 12 \text{ \AA}^{-1}$) due to the restricted opening of DACs, the $S(q)$ and $G(r)$ are reliable according to their consistent feature with the high-energy PDF of the ambient samples ($q_{\text{max}} \approx 30 \text{ \AA}^{-1}$, see Fig. 1).

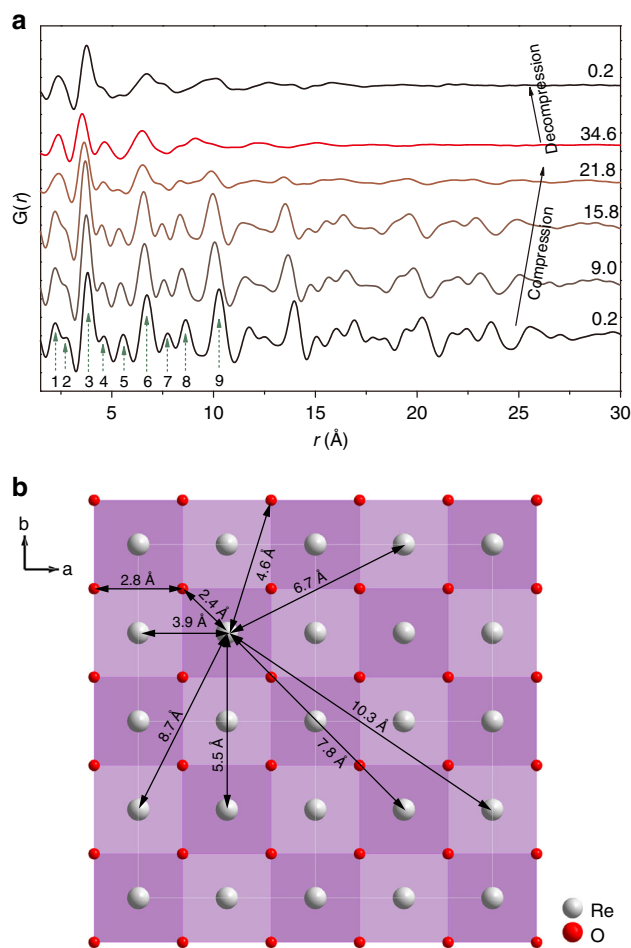


Fig. 4 Structure evolution in real space. **a** Selected pair distribution function (PDF) of the (Ce,La,Pr,Sm,Y)O HEO during compression and decompression at room temperature. The numbers denote the peaks for different atomic pairs. **b** The structure model for the cubic structure of (Ce,La,Pr,Sm,Y)O HEO. The distances between different atom pairs are shown with arrows, which correspond to peaks marked by numbers in **a**. Different colors of the cubes represent different atomic layers

The CaF_2 -type structure of the (Ce,La,Pr,Sm,Y)O HEO consists of REO_8 hexahedrons (cubes) with a cubic close-packed arrangement, in which each RE atom is surrounded by eight O atoms forming eight RE–O bonds. All the REO_8 cubes connect with each other by sharing one edge. The RE–O bonds inside REO_8 cubes are quite rigid and remain almost constant during compression up to ~ 30 GPa, while all the other longer atomic distances between different REO_8 cubes considerably decrease with increasing pressure (Fig. 5a, b). With accurately determined bond lengths by fitting the peaks in $G(r)$, the pressure dependence of bond angles inside one cube $\theta_{\text{O-RE-O}}$ and between the nearest cubes $\theta_{\text{RE-O-RE}}$ can be calculated as shown in Fig. 5c. During compression, both of the average $\theta_{\text{O-RE-O}}$ and $\theta_{\text{RE-O-RE}}$ decrease continuously. The sample volume compression is achieved mainly by bending the bond angles. Eventually, the long-range coherence between REO_8 cubes breaks down when the pressure is above the mechanical instability limit, hence, leading to amorphization.

Upon decompression, both $S(q)$ and $G(r)$ seem to retain their amorphous feature. However, regardless of the peak shifting due to elastic recovery, the $S(q)$ pattern is slightly different from the high-pressure pattern at 34.6 GPa especially in the range from 2.5 to 4.5 \AA^{-1} . This result suggests that the low-pressure recovered

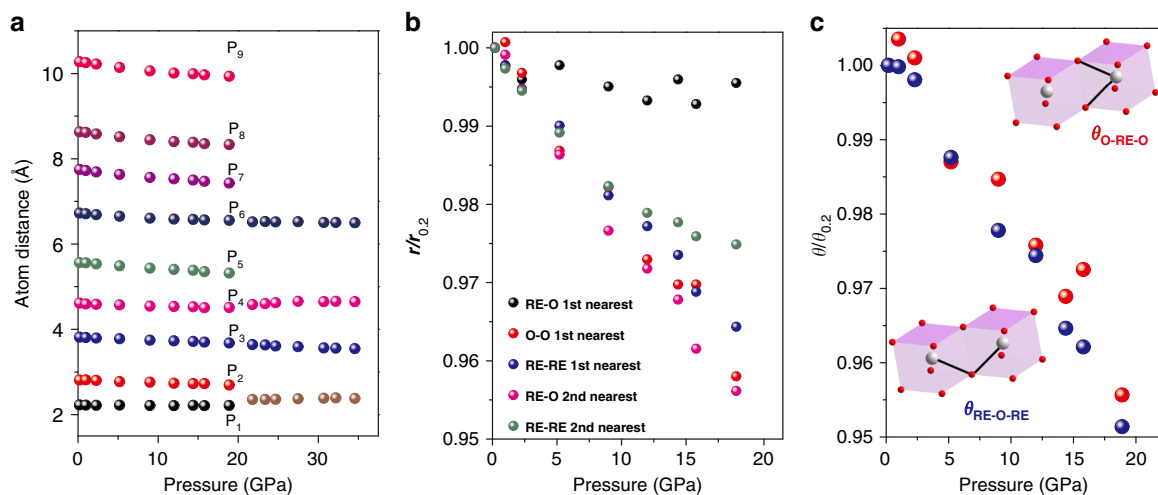


Fig. 5 Pressure dependence of atomic pair distances and bond angles. **a** The pressure dependence of the atomic pair distances associated with the peaks in Fig. 4a. The error bars are smaller than the symbol sizes. **b** Normalized atomic pair distance of the major peaks in Fig. 4a before amorphization. **c** The pressure dependence of the two representative bond angles $\theta_{\text{O-RE-O}}$ (in one cube) and $\theta_{\text{RE-O-RE}}$ (between the nearest-neighbor cubes)

state is different from the high-pressure amorphous state. $G(r)$ also looks different after decompression. To clarify the structure change after the pressure release, HRTEM was performed on the recovered samples (Supplementary Fig. 3). The recovered sample mostly remains in a highly disordered amorphous state, but some fine nano-grains of the initial CaF_2 crystalline structure show up in the amorphous matrix. Therefore, a composite HEO with amorphous matrix plus some super fine nanocrystals has been synthesized via compression and the following decompression processes of the initial HEO.

The structural stability of the prototype (Ce,La,Pr,Sm,Y)O HEO has been studied from room temperature to ~ 1023 K at ambient pressure, but no amorphization or any other phase transition has ever been observed⁷. A symmetry lowering phase transition from $Fm\bar{3}m$ to $Ia\bar{3}$ space groups was observed only after calcination at 1273 K for 1 h⁷. Its phase stability under high-pressure was not explored before. In contrast, the phase transitions under high-pressure have been extensively studied in all of its constituent rare-earth oxides in nano or bulk forms, for example, Ce_2O_3 ³⁰, CeO_2 ^{30–32}, La_2O_3 ³³, Pr_2O_3 ³⁴, PrO_2 ³⁵, Sm_2O_3 ³⁶, and Y_2O_3 ^{37–39}. Among them, however, the PIA process was only observed in the Y_2O_3 nanoparticles with sizes < 16 nm³⁹. The Y_2O_3 nanoparticles have a cubic structure (space group: $Ia\bar{3}$) at ambient condition, which consists of YO_6 octahedra as the building block. The YO_6 octahedra are less compressible than the global Y_2O_3 lattice. Therefore, during compression, the densification is mainly carried by bending the polyhedral-linking angles to squeeze the space between the octahedra. When the bending is beyond a critical mechanical limit, the structure collapses and transforms into an amorphous state at ~ 25 GPa. Smaller grain size usually results in higher transition pressures for the PIA³⁹. This mechanism was also proposed for the PIA in many other polyhedral-linked materials such as the prototype oxide, SiO_2 ⁴⁰. PIA refers to an unusual phenomenon with direct transformation of a crystal into an amorphous solid, which was firstly reported in ice I_h , afterwards, has attracted intense interest and observed in a wide range of substances⁴¹. Our results in this work demonstrate that a similar mechanism proposed for PIA in conventional oxides may also hold for the case of the chemically much more complex HEO according to the bonding length and angle changes during compression.

The (Ce,La,Pr,Sm,Y)O HEO consists of five cations with different ionic radii, and more importantly different oxidation

states (valence), e.g., 3+ oxidation for La, Sm, Y; 4+ for Ce, and mixed multiple oxidation states (3+ and 4+) for Pr^{29,42}. CeO_2 is believed to be the critical component which stabilizes the single-phase of the HEO and provides a CaF_2 -type host lattice for the other cations. However, except Ce^{4+} and Pr^{4+} , the other rare-earth cations including partial Pr are present in the 3+ oxidation states. To keep the charge balance of the system, high-level oxygen vacancies are naturally required and created in the (Ce,La,Pr,Sm,Y)O HEO²⁹. Therefore, the oxygen vacancies and cations valence are closely associated in the HEO. The different ionic radii and a high level of oxygen vacancies could both contribute to the lattice distortion in the initial (Ce,La,Pr,Sm,Y)O HEO sample which may be the reason for the slight deviation of the bond angles from ideal values. However, according to the $G(r)$ data, the first atomic shell consists of RE–O bonding is rigid without obvious bond shrinkage during compression. Therefore, the size of different cations may not change much as well during the entire compression. On the other hand, the atoms (both the RE cations and other oxygen anions) surrounding a given oxygen vacancy site are expected to displace from their original positions in a perfect lattice, which could also result in bond angle deviations. Therefore, the behavior of oxygen vacancies during compression could dramatically affect the structure evolution under high-pressure.

In situ high-pressure Raman spectroscopy. Oxygen vacancies of the (Ce,La,Pr,Sm,Y)O HEO can be readily detected by Raman spectroscopy²⁹. Thus, we performed in situ high-pressure Raman spectroscopy (Fig. 6) on the (Ce,La,Pr,Sm,Y)O HEO in a DAC (details can be found in the “Methods” section), which could provide another indicator of the development of the lattice distortion of (Ce,La,Pr,Sm,Y)O HEO during compression. The F_{2g} symmetric vibration mode of the eight-fold RE–O bond in the (Ce,La,Pr,Sm,Y)O which is typically located at ~ 450 cm^{-1} is barely visible. The Raman peak weakening for F_{2g} can be explained by the symmetry breaking (the severe local lattice distortion) in the (Ce,La,Pr,Sm,Y)O caused by chemical disorder²⁹. The Raman peak at ~ 600 cm^{-1} (V_O band) at ambient conditions was confirmed to be the characteristic peak of oxygen vacancies of the (Ce,La,Pr,Sm,Y)O HEO which is relatively strong at ambient conditions. During compression, the V_O band shifts to higher wavenumbers, and its intensity decreases significantly until

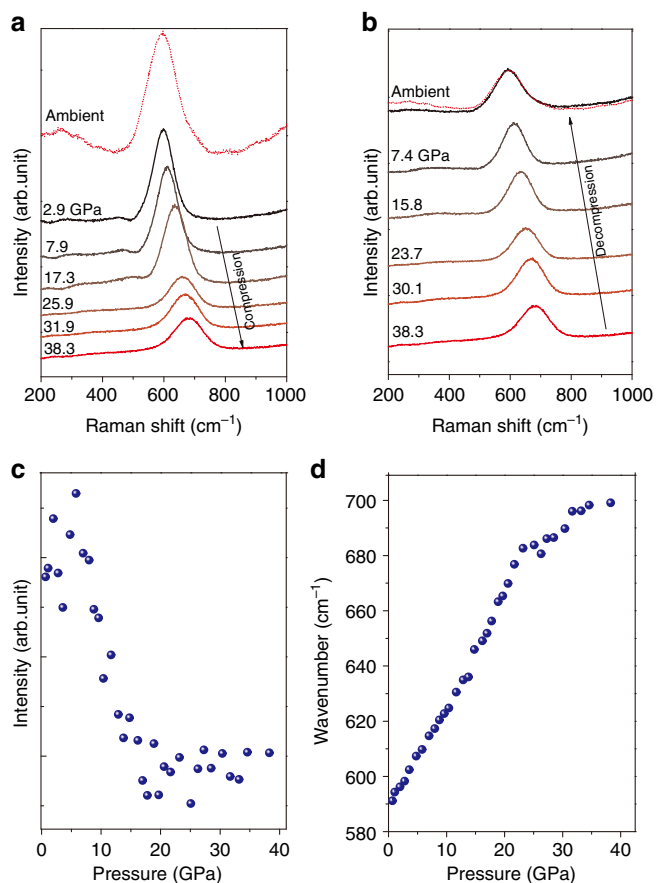


Fig. 6 In situ high-pressure Raman spectra. In situ high-pressure Raman spectra of the (Ce,La,Pr,Sm,Y)O HEO in a DAC during compression **a** and decompression **b** at room temperature. The dotted line is the spectrum of the initial sample collected outside of the DAC at ambient conditions (the intensity was rescaled by a factor of 0.53). The peak intensity and peak width of the recovered sample almost return back to the initial values before compression. The Raman peak position **c** and intensity **d** as a function of pressure upon compression. A dramatic slope change can be found at ~20 GPa in both **c** and **d**

~20 GPa. This observation indicates that the oxygen vacancies may change their distribution and concentration during compression below 20 GPa, which could be associated with the relatively large compressibility of the vacancy spot and also the tunable valences of the Pr^{3+} to Pr^{4+} during compression^{43,44}. Above ~20 GPa, the amorphization is completed, therefore, it is reasonable that the intensity of V_O band remained almost constant. Naturally, the bond angles and local lattice distortion will be altered by the collapse of oxygen vacancies and oxidation state-induced change in the cationic radii of Pr cation, which is consistent with the results obtained by in situ high-pressure XRD. During decompression, the intensity and peak position of the V_O band gradually recovered to the initial values. This result suggests that the collapse of oxygen vacancies may be caused by elastic deformation and the change of cations valence during compression, which is reversible upon decompression and likely independent of the lattice disorder⁴⁵. To clarify the role of each constituent element of this HEO in its structural evolution under high-pressure, element-specific technique, such as x-ray absorption spectroscopy (XAS) is needed. However, in situ high-pressure XAS especially extended x-ray absorption fine structure (EXAFS) is challenging to the (Ce,La,Pr,Sm,Y)O HEO in a DAC due to the either too high X-ray energy (K-edge) for the thin

samples (<20 μm) or too low X-ray energy (L-III edge) for the thick diamond anvils (~2.4 mm), and too close absorption edges of some constituent elements.

During decompression, most of the amorphous state could be kinetically retained by the possible large barrier required for the recovery of the initial cubic crystalline structure. During heating at ambient pressure, the (Ce,La,Pr,Sm,Y)O HEO will have a phase transition from the fluorite-type to the bixbyite-type phase transition with lower symmetry⁷. However, we did not observe this polymorphic crystal-to-crystal transition under high-pressure and room temperature. Instead, an amorphization takes place. We speculate that the crystal-to-crystal transitions may be hindered by a large energy barrier in this system, therefore, we also performed in situ laser heating XRD measurements at high-pressure (more experimental details can be found in ref. ⁴⁶) on the (Ce,La,Pr,Sm,Y)O HEO (Supplementary Fig. 4). Thermodynamically more stable crystal phases (do not match the bixbyite-type phase) do exist at pressures before the amorphization and after the amorphization if the sample is heated above ~1100 K. A possible phase separation also cannot be neglected under high-pressure and high-temperature. More efforts are needed to solve the structure of the high-pressure and high-temperature crystalline phase in the future.

Pressure tuning of band gap. Since the structure of (Ce,La,Pr,Sm,Y)O HEO is extremely susceptible to pressure, we expected tunable properties during compression as well. In this work, we studied its band gap as a function of pressure using in situ high-pressure UV-vis spectroscopy. The indirect and direct gap values were obtained by fitting the absorption spectra using the Tauc relation (Fig. 7)²⁹, i.e., $[F(R_\infty) \cdot h\nu]^{1/n} = A \cdot (h\nu - E_g)$, where $F(R_\infty)$ is the Kubelka-Mubelka-Munk function, h is the Planck's constant, ν is the frequency, A is a constant, and E_g is the band gap energy. Details of the fitting of E_g can be found in Supplementary Fig. 5. Before amorphization (<~16 GPa), the sample exhibits enhanced band gap with increasing pressure, this is unusual compared to the typical band gap decreasing in traditional oxides during compression^{47,48}. It may be caused by the accumulated lattice distortion energy. Above 16 GPa, once the sample starts amorphization, the band gap turns to decrease sharply until the amorphization completes at ~22 GPa. Above 22 GPa, the band gap increases with pressure again. The complex pressure dependence of the band gap observed in the (Ce,La,Pr,Sm,Y)O HEO is consistent with its structure evolution during compression revealed by XRD. The enhanced band gap below 16 GPa and above 22 GPa during compression seems to be an intrinsic feature in both the cubic crystalline and amorphous states during compression. The drop of band gap between 16 and 22 GPa is likely associated with the amorphization process, which may be attributed to the distortion (strain) release due to the amorphization (bond breaking and atom rearrangement). Although there is no reliable data collected during decompression in this work due to our experimental issue, we expected a partially reversible band gap change during decompression according to its atomic structure evolution. More tunable functional properties of the HEOs under high-pressure are promising and worth exploring in the future. The band gap of the initial (Ce,La,Pr,Sm,Y)O HEO sample (direct band gap: 2.06 eV, indirect band gap: 1.52 eV) is much narrower than the parent CeO_2 sample (direct band gap: 3.17 eV, indirect band gap: 2.76 eV). The origin for the band gap narrowing in the (Ce,La,Pr,Sm,Y)O HEO is not very clear. The tunable behavior of the band gap over a relatively broad range (changes by 9% for direct band gap and 24% for the indirect band gap from ~1 to ~10 GPa) achieved under high-pressure could

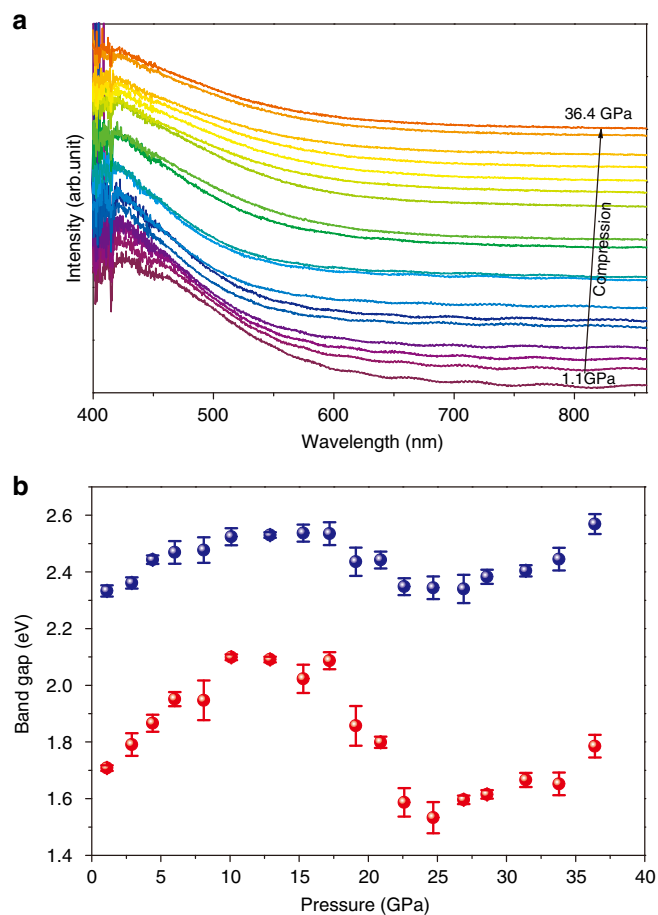


Fig. 7 In situ UV-vis absorption spectra. **a** In situ high-pressure UV-vis absorption spectra of the (Ce,La,Pr,Sm,Y)O HEO upon compression. **b** Fitted direct (blue balls) and indirect (red balls) band gap as a function of pressure. The error bars are from the linear fitting of the absorption spectra according to the Tauc plots

help to understand its underlying mechanism and even achieve band gap engineering via high-pressure treatment^{49,50}.

Discussion

The structural stability of the (Ce,La,Pr,Sm,Y)O HEO is studied during compression up to ~35 GPa using in situ high-pressure synchrotron radiation XRD. A crystal to amorphous phase transition is observed which starts at ~16 GPa and completes at ~22 GPa. PDF analysis reveals the microscopic mechanism of the amorphization, which is attributed to the breakdown of long-range connectivity between REO₈ cubes caused by continuous bending/tilting of bond angles inside and between the REO₈ cubes. The atomic distortion caused by chemical disorder and high-level oxygen vacancies is suggested to exist even in the initial crystalline HEO (the bond angles deviate from ideal values) and is extremely sensitive to pressure. The development of lattice distortion plays a vital role in the amorphization and band gap tuning. These results suggest that although the HEOs are very stable at high temperatures and ambient pressure, they are susceptible to pressure loading. Their properties could be highly tunable under high-pressure as well. Pressure-induced transformation directly from crystalline states to the amorphous solid states at temperatures below the melting point or glass transition temperature is well-known as the “PIA” phenomenon since the 1980s in various materials⁵¹. However, it has never been observed in the multicomponent HEO systems before. For HEO, the PIA

also means the direct transition from ceramics to glasses, which could lead to the development of useful nano-ceramic-glass composite materials with tunable properties. Since the HEOs may commonly involve severe lattice distortion due to cation size mismatch and/or a high level of oxygen vacancies, we expect interesting pressure-induced transitions including PIA in other HEOs.

Methods

In situ high-pressure synchrotron XRD measurements. In situ high-pressure angle-dispersive XRD experiments were mainly performed at the GSECARS beamline 13-ID-D, Advanced Photon Source (APS), Argonne National Laboratory (ANL). A monochromatic X-ray beam with a wavelength of 0.3218 Å was focused by a Kirkpatrick-Baez (KB) mirror system down to ~2.5 × 3.5 μm² at the rotation center of the sample stage. The detector was a Mar165 charge-coupled device (CCD). The position and orientation of the detector to the X-ray beam were calibrated using the diffraction pattern of a LaB₆ standard. High-pressure was generated using a symmetric DAC with a culet size of ~400 μm in diameter. The gasket was T301 stainless steel that was pre-indented to ~20 GPa. A hole with a diameter of ~150 μm was drilled to serve as the sample chamber by a laser drilling system at the center of the gasket indent. The powder was pre-pressed into a thin pellet and cut into flakes with proper sizes for DACs. Then, the tiny flake was loaded into a DAC along with a tiny ruby ball and Au foil beside the samples to calibrate pressure. Methonal:ethonal = 4:1 (volume ratio) mixture was used as the pressure-transmitting medium. The background scattering was collected at each pressure point by shining the X-ray beam on the empty area inside the sample chamber, which only passed through the pressure medium and two diamond anvils. The exposure time was set at 10 s for normal XRD. For PDF measurements, the exposure time for each pattern was set to be 30 s. One-dimensional (1D) XRD patterns were obtained by integrating the 2D patterns along the azimuth angle from 0° to 360° with the Dioptas software⁵². The resulting diffraction patterns were refined using the GSAS package.

In situ high-pressure Raman spectroscopy measurements. Raman spectroscopy measurements were conducted using a Renishaw inVia spectrometer with a 532 nm laser excitation. High-pressure was generated using a symmetric DAC with a culet size of ~400 μm in diameter. The powder sample was pre-pressed into a pellet and then loaded into a DAC, along with two tiny ruby balls beside the samples to calibrate pressure. Silicone oil was used as the pressure-transmitting medium. The exposure time for each pattern was ~50 s. The signal from background was obtained by shining a laser beam on the spot inside the sample chamber but away from the sample.

In situ high-pressure UV-vis spectroscopy measurements. UV-vis spectroscopy measurements were conducted using an Ocean Optics DH-2000-BAL spectrometer. High-pressure was generated using a symmetric DAC with a culet of ~300 μm in diameter. The powder sample was pre-pressed into thin flakes with right thickness and then loaded into a DAC, along with two tiny ruby balls beside the sample to calibrate pressure. Silicone oil was used as the pressure-transmitting medium. Each spectrum was collected for 1 s with wavelength ranged from 180 to 860 nm. The background signal was collected at the empty area (with pressure medium only) of the sample chamber.

HRTEM. The powder samples were dispersed in ethyl alcohol and picked up using a holey carbon grid. HRTEM experiments were carried out using the chromatic-aberration-corrected TEM (ACAT) at ANL with an image corrector to correct both spherical and chromatic aberrations. An accelerating voltage of 80 kV was used to minimize the possible electron irradiation effect on the sample structure.

Data availability

The data that support the findings of this study are available from the corresponding author upon reasonable request.

Received: 24 June 2019; Accepted: 5 September 2019;

Published online: 27 September 2019

References

- Cantor, B., Chang, I. T. H., Knight, P. & Vincent, A. J. B. Microstructural development in equiatomic multicomponent alloys. *Mater. Sci. Eng. A* 375–377, 213–218 (2004).
- Yeh, J. W. et al. Nanostructured high-entropy alloys with multiple principal elements: novel alloy design concepts and outcomes. *Adv. Eng. Mater.* 6, 299–303 (2004).

3. Singh, S., Wanderka, N., Murty, B. S., Glatzel, U. & Banhart, J. Decomposition in multi-component AlCoCrCuFeNi high-entropy alloy. *Acta Mater.* **59**, 182–190 (2011).
4. Zhang, Y., Yang, X. & Liaw, P. K. Alloy design and properties optimization of high-entropy alloys. *JOM* **64**, 830–838 (2012).
5. Zhang, Y. et al. Microstructures and properties of high-entropy alloys. *Prog. Mater. Sci.* **61**, 1–93 (2014).
6. Rost, C. M. et al. Entropy-stabilized oxides. *Nat. Commun.* **6**, 8485 (2015).
7. Djenadic, R. et al. Multicomponent equiatomic rare earth oxides. *Mater. Res. Lett.* **5**, 102–109 (2016).
8. Sarkar, A. et al. Rare earth and transition metal based entropy stabilised perovskite type oxides. *J. Eur. Ceram. Soc.* **38**, 2318–2327 (2018).
9. Jiang, S. et al. A new class of high-entropy perovskite oxides. *Scr. Mater.* **142**, 116–120 (2018).
10. Dąbrowa, J. et al. Synthesis and microstructure of the (Co,Cr,Fe,Mn,Ni) 3 O 4 high entropy oxide characterized by spinel structure. *Mater. Lett.* **216**, 32–36 (2018).
11. Bérandan, D., Franger, S., Drago, D., Meena, A. K. & Drago, N. Colossal dielectric constant in high entropy oxides. *Phys. Status Solidi Rapid Res Lett.* **10**, 328–333 (2016).
12. Bérandan, D., Franger, S., Meena, A. K. & Drago, N. Room temperature lithium superionic conductivity in high entropy oxides. *J. Mater. Chem. A* **4**, 9536–9541 (2016).
13. Hu, W. et al. Electron-pinned defect-dipoles for high-performance colossal permittivity materials. *Nat. Mater.* **12**, 821–826 (2013).
14. Rost, C. M. Entropy-Stabilized Oxides: Explorations of a Novel Class of Multicomponent Materials. Ph.D. dissertation, North Carolina State University (2016).
15. Sarkar, A. et al. High entropy oxides for reversible energy storage. *Nat. Commun.* **9**, 3400 (2018).
16. Qiu, N. et al. A high entropy oxide (Mg_{0.2}Co_{0.2}Ni_{0.2}Cu_{0.2}Zn_{0.2}O) with superior lithium storage performance. *J. Alloy. Compd.* **777**, 767–774 (2019).
17. Xu, W. et al. Entropy-driven mechanochemical synthesis of polymetallic zeolitic imidazolate frameworks for CO₂ fixation. *Angew. Chem. Int. Ed.* **58**, 5018–5022 (2019).
18. Wang, L. et al. Abundant polymorphic transitions in the Al_{0.6}CoCrFeNi high-entropy alloy. *Mater. Today Phys.* **8**, 1–9 (2019).
19. Dupuy, A. D., Wang, X. & Schoenung, J. M. Entropic phase transformation in nanocrystalline high entropy oxides. *Mater. Res. Lett.* **7**, 60–67 (2019).
20. Mao, H.-K. et al. Recent advances in high-pressure science and technology. *Matter Radiat. Extremes* **1**, 59–75 (2016).
21. Wu, H. et al. Pressure-driven assembly of spherical nanoparticles and formation of 1D-nanostructure arrays. *Angew. Chem. Int. Ed.* **49**, 8431–8434 (2010).
22. Wu, B. Y., Xiao, Y., Chen, G., Liu, C. T. & Lu, Z. Bulk metallic glass composites with transformation-mediated work-hardening and ductility. *Adv. Mater.* **22**, 2770–2773 (2010).
23. Jordá, J. L. et al. Synthesis of a novel zeolite through a pressure-induced reconstructive phase transition process. *Angew. Chem. Int. Ed.* **52**, 10458–10462 (2013).
24. Zhang, F. et al. Polymorphism in a high-entropy alloy. *Nat. Commun.* **8**, 15687 (2017).
25. Tracy, C. L. et al. High pressure synthesis of a hexagonal close-packed phase of the high-entropy alloy CrMnFeCoNi. *Nat. Commun.* **8**, 15634 (2017).
26. Zhang, F. X. et al. Pressure-induced fcc to hcp phase transition in Ni-based high entropy solid solution alloys. *Appl. Phys. Lett.* **110**, 011902 (2017).
27. Yu, P. F. et al. Pressure-induced phase transitions in HoDyYGdNb high-entropy alloy. *Mater. Lett.* **196**, 137–140 (2017).
28. Cheng, B. et al. Pressure-induced phase transition in the AlCoCrFeNi high-entropy alloy. *Scr. Mater.* **161**, 88–92 (2019).
29. Sarkar, A. et al. Multicomponent equiatomic rare earth oxides with a narrow band gap and associated praseodymium multivalency. *Dalton Trans.* **46**, 12167–12176 (2017).
30. Lipp, M. J. et al. Comparison of the high-pressure behavior of the cerium oxides Ce₂O₃ and CeO₂. *Phys. Rev. B* **93**, 064106 (2016).
31. Wang, Q. et al. Unusual compression behavior of nanocrystalline CeO(2). *Sci. Rep.* **4**, 4441 (2014).
32. Liu, B. et al. High-pressure studies on CeO₂ nano-octahedrons with a (111)-terminated surface. *J. Phys. Chem. C* **115**, 4546–4551 (2011).
33. McClure, J. P. High Pressure Phase Transitions in the Lanthanide Sesquioxides. Ph.D dissertation, University of Nevada Las Vegas (2009).
34. Saranya, L. et al. High pressure structural studies on nanophase praseodymium oxide. *Physica B* **449**, 109–112 (2014).
35. Gerward, L. et al. Bulk modulus of CeO₂ and PrO₂—an experimental and theoretical study. *J. Alloy. Compd.* **400**, 56–61 (2005).
36. Jiang, S., Liu, J., Lin, C., Li, X. & Li, Y. High-pressure x-ray diffraction and Raman spectroscopy of phase transitions in Sm₂O₃. *J. Appl. Phys.* **113**, 113502 (2013).
37. Skrikanth, V., Sato, A., Yoshimoto, J., Kim, J. H. & Ikegami, T. Synthesis and crystal structure study of Y₂O₃ high-pressure polymorph. *Cryst. Res. Technol.* **29**, 981–984 (1994).
38. Halevy, I. et al. Pressure-induced structural phase transitions in Y₂O₃ sesquioxide. *J. Phys.: Conf. Ser.* **215**, 012003 (2010).
39. Wang, L. et al. Size-dependent amorphization of nanoscale Y₂O₃ at high pressure. *Phys. Rev. Lett.* **105**, 095701 (2010).
40. Hemley, R. J., Jephcoat, A. P., Mao, H. K., Ming, L. C. & Manghnani, M. H. Pressure-induced amorphization of crystalline silica. *Nature* **334**, 52–54 (1988).
41. Machon, D., Meersman, F., Wilding, M. C., Wilson, M. & McMillan, P. F. Pressure-induced amorphization and polyamorphism: inorganic and biochemical systems. *Prog. Mater. Sci.* **61**, 216–282 (2014).
42. Sarkar, A. et al. Nanocrystalline multicomponent entropy stabilised transition metal oxides. *J. Eur. Ceram. Soc.* **37**, 747–754 (2017).
43. Brodholt, J. P. Pressure-induced changes in the compression mechanism of aluminous perovskite in the Earth’s mantle. *Nature* **407**, 620 (2000).
44. Bradley, J. A. et al. 4f electron delocalization and volume collapse in praseodymium metal. *Phys. Rev. B* **85**, 100102 (2012).
45. Zeng, Q. S. et al. Origin of pressure-induced polyamorphism in Ce₇₅Al₂₅ metallic glass. *Phys. Rev. Lett.* **104**, 105702 (2010).
46. Zeng, Z. et al. Synthesis of quenchable amorphous diamond. *Nat. Commun.* **8**, 322 (2017).
47. Cheng, B. et al. Pressure-induced metallization and amorphization in VO₂(A) nanorods. *Phys. Rev. B* **93**, 184109 (2016).
48. McWilliams, R. S. et al. Phase transformations and metallization of magnesium oxide at high pressure and temperature. *Science* **338**, 1330 (2012).
49. Li, Q. et al. High-pressure band-gap engineering in lead-free Cs₂AgBiBr₆ double perovskite. *Angew. Chem. Int. Ed.* **56**, 15969–15973 (2017).
50. Anand, G., Wynn, A. P., Handley, C. M. & Freeman, C. L. Phase stability and distortion in high-entropy oxides. *Acta Mater.* **146**, 119–125 (2018).
51. Machon, D. & Mélinon, P. Size-dependent pressure-induced amorphization: a thermodynamic panorama. *PCCP* **17**, 903–910 (2015).
52. Prescher, C. & Prakapenka, V. B. DIOPTAS: a program for reduction of two-dimensional X-ray diffraction data and data exploration. *High Press. Res.* **35**, 223–230 (2015).

Acknowledgements

This research was supported by the National Natural Science Foundation of China (No. 51871054, U1930401), the Fundamental Research Funds for the Central Universities, and the Deutsche Forschungsgemeinschaft (DFG) under contract number HA 1344/43-1. We would like to thank Dr. Liang Wang for his help with the PDF measurement at ambient conditions and Dr. Lin Wang for his help with the ultraviolet-visible absorption spectroscopy measurement. The usage of the beamline 13-ID-D (GeoSoilEnviroCARS) at APS was supported by the National Science Foundation (NSF)-Earth Sciences (EAR-1634415) and Department of Energy (DOE)-GeoSciences (DE-FG02-94ER14466). The use of APS and Center for Nanoscale Materials (CNM), an Office of Science user facility, was supported by the DOE, Office of Science, Office of Basic Energy Sciences, under contract no. DE-AC02-06CH11357. Part of this work used the beamline 16-ID-B of APS, USA, 15U1 of SSRF, China, and also the beamline 12.2.2, Advanced Light Source (ALS), which is a DOE Office of Science User Facility under contract no. DE-AC02-05CH11231.

Author contributions

Q.S.Z. and H.H. initiated this research project. Q.S.Z. designed the experiments. A.S., R.D., B.Y.C. and H.B.L. synthesized and characterized the initial sample. H.B.L., Z.D.Z., F.Z., X.H.C., L.J.T., V.P., E.G. and Q.S.Z. performed the synchrotron radiation x-ray experiments. J.G.W., H.B.L., F.Z. and Q.S.Z. carried out the HRTEM experiments. B.Y.C., H.B.L., Z.D.Z. and Q.S.Z. analyzed the data. Q.S.Z. and B.Y.C. wrote the paper. All authors participated in the discussion and interpretation of the results.

Competing interests

The authors declare no competing interests.

Additional information

Supplementary information is available for this paper at <https://doi.org/10.1038/s42004-019-0216-2>.

Correspondence and requests for materials should be addressed to Q.Z.

Reprints and permission information is available at <http://www.nature.com/reprints>

Publisher’s note Springer Nature remains neutral with regard to jurisdictional claims in published maps and institutional affiliations.



Open Access This article is licensed under a Creative Commons Attribution 4.0 International License, which permits use, sharing, adaptation, distribution and reproduction in any medium or format, as long as you give appropriate credit to the original author(s) and the source, provide a link to the Creative Commons license, and indicate if changes were made. The images or other third party material in this article are included in the article's Creative Commons license, unless indicated otherwise in a credit line to the material. If material is not included in the article's Creative Commons license and your intended use is not permitted by statutory regulation or exceeds the permitted use, you will need to obtain permission directly from the copyright holder. To view a copy of this license, visit <http://creativecommons.org/licenses/by/4.0/>.

© The Author(s) 2019